



## Design of graded lattice structure with optimized mesostructures for additive manufacturing



Yiqiang Wang <sup>a</sup>, Lei Zhang <sup>c</sup>, Stephen Daynes <sup>d</sup>, Hongying Zhang <sup>c</sup>, Stefanie Feih <sup>d</sup>, Michael Yu Wang <sup>a,b,\*</sup>

<sup>a</sup> Department of Mechanical and Aerospace Engineering, Hong Kong University of Science and Technology, Clear Water Bay, Kowloon, Hong Kong

<sup>b</sup> Department of Electronic and Computer Engineering, Hong Kong University of Science and Technology, Clear Water Bay, Kowloon, Hong Kong

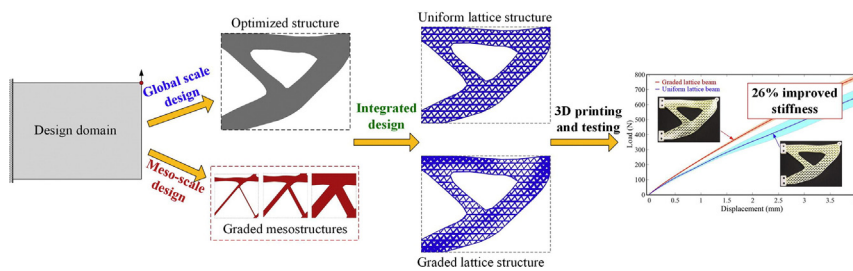
<sup>c</sup> Department of Mechanical Engineering, National University of Singapore, 117575, Singapore

<sup>d</sup> Joining Technology Group, Singapore Institute of Manufacturing Technology (SIMTech), 2 Fusionopolis Way, 138634, Singapore

### HIGHLIGHTS

### GRAPHICAL ABSTRACT

- A design method is developed for graded lattice structures.
- Geometries of global structure, lattice meso-structures and their spatial layout are optimized.
- Experimental testing shows 24% improved stiffness of optimized graded lattice structures than uniform ones.



### ARTICLE INFO

#### Article history:

Received 6 October 2017

Received in revised form 17 December 2017

Accepted 7 January 2018

Available online 11 January 2018

#### Keywords:

Additive manufacturing

Topology optimization

Lattice structure

Graded lattice

Level set method

### ABSTRACT

Additive manufacturing (AM) enables fabrication of multiscale cellular structures as a whole part, whose features can span several dimensional scales. Both the configurations and layout pattern of the cellular lattices have great impact on the overall performance of the lattice structure. In this paper, we propose a novel design method to optimize cellular lattice structures to be fabricated by AM. The method enables an optimized load-bearing solution through optimization of geometries of global structures and downscale mesostructures, as well as global distributions of spatially-varying graded mesostructures. A shape metamorphosis technology is incorporated to construct the graded mesostructures with essential interconnections. Experimental testing is undertaken to verify the superior stiffness properties of the optimized graded lattice structure compared to the baseline design with uniform mesostructures.

© 2018 Elsevier Ltd. All rights reserved.

### 1. Introduction

Lattice structures have attracted tremendous attention from researchers and engineers for multifunctional design opportunities [1]

as well as their significant potential for a wide range of lightweight applications [2], e.g. in aerospace, automotive and biomechanical engineering areas. Classically, lattice structures can be divided to be periodic or stochastic from their layout patterns. Extensive studies have been carried out to demonstrate the superior performance of periodic lattices compared to stochastic ones. For example, the periodic octet-truss lattice has been demonstrated to gain efficient stiffness-to-weight and strength-to-weight benefits because of its stretching-dominated behavior [3]. However, the mechanical behavior of lattice structures could be quite different when their feature sizes are

\* Corresponding author at: Department of Mechanical and Aerospace Engineering, Hong Kong University of Science and Technology, Clear Water Bay, Kowloon, Hong Kong.

E-mail addresses: [leizhang@u.nus.edu](mailto:leizhang@u.nus.edu) (L. Zhang), [\(S. Daynes\)](mailto:dayness@SIMTech.a-star.edu.sg), [hongying\\_zhang@u.nus.edu](mailto:hongying_zhang@u.nus.edu) (H. Zhang), [feihs@SIMTech.a-star.edu.sg](mailto:feihs@SIMTech.a-star.edu.sg) (S. Feih), [mywang@ust.hk](mailto:mywang@ust.hk) (M.Y. Wang).

comparable to the length scale of the global structure, referred to as mesostructures. In this instance, lattices can no longer be taken as microarchitected materials but are designed as primary load-bearing parts.

During the past decade, topology optimization has become a favorite to optimize the layout pattern of variable mesostructures to create novel cellular lattice structures (CSs). In general, most methods make use of lattices comprised of beams/trusses [4], which can work effectively at a low relative density with members of small bar diameters or wall thicknesses. However, the approach may result in severe limitations when generating designs of shell-like or/and solid features with higher stiffness requirements. Some other studies realized design process by adopting a set of mesostructures with retained topologies, in which their relative densities and effective properties can be characterized by a set of explicit geometrical parameters, such as the edge lengths of rectangular holes [5] or the radii of central circular holes [6]. But the use of conventional lattice structures may not bring out full mechanical advantages of optimized CSs [7]. On the other hand, designing the geometry of a unit cell can generate cellular materials of tailored properties [8], which can further be used for infilling the macrostructure [9]. However, finding and fabricating optimal cellular materials for prescribed structures still remains as an open area [10].

For pursuing the best performance of CSs, it is preferable to carry out a design process at two length scales [11–13]. Both the topological configurations as well as the distribution patterns of the constituent mesostructures should be optimized in an integrated manner. With regard to specific load and boundary conditions, the optimized mesostructures provide directional stiffness to enhance structural load-bearing capabilities. Although some previous studies have focused on the design of uniform mesostructures (UMs) (e.g. [14, 15]), it is more beneficial to take into consideration the optimization of spatially-varying mesostructures, because of their expanded design space [16–19].

Typically, two issues are encountered when numerically designing CSs involving varying mesostructures. The first one is related to the high computational cost, which is mainly caused by solving the homogeneous equations for a huge number of non-periodic mesostructures to evaluate their effective properties. This problem can be partially addressed by developing parallel multiscale computational algorithms. The other more critical issue is the lack of connectivity between two neighboring optimized mesostructures, due to the decoupled design process [12]. The disconnected regions yield unconstrained members that are unable to transfer load. Some existing studies tackled this issue by developing a non-local multiscale analysis model [16] or using a refined analysis model [13, 14], but this may still be computationally expensive. To this end, an effective and efficient multiscale CS design method is still in high demand. Furthermore, experimental verification of the superior mechanical performance of CSs with spatially-varying mesostructures compared to the baseline designs with uniform mesostructures is still quite limited to date [6, 20].

Advancement of additive manufacturing (AM) process gives engineers and designers great freedoms to fabricate novel structures with complex geometries, benefiting from the layer-by-layer material addition process [21]. It is straightforward to combine topology optimization and AM for producing high-performance optimized engineering structures [22]. Moreover, AM has shown its strong capabilities of fabricating different types of microarchitectures, which could be composed of either plastics [23], metals [24–27], ceramics [28] or bi-materials [29]. Recently, several research groups printed graded lattices and tested their overall performance, e.g. in [30]. In particular, AM enables the direct fabrication of multiscale CSs as a whole part without any additional assembly process [31]. In addition, AM technologies are largely unconstrained by the design complexity of a CS.

In this study, we propose a novel structural design methodology for optimizing graded lattice structures for AM. Here, we incorporate a special class of varying mesostructures, the graded mesostructures (GMs),

into the design. The ‘graded’ means that the optimized mesostructures have similar topological features, but exhibit varying mechanical behaviors. In the proposed design framework, the CS geometry, the mesostructure configuration as well as the layout pattern of the varying GMs are all optimized in a subsequent optimization flow. In order to construct GMs for any geometry covering a wide range of mechanical properties, a configuration interpolation technology is developed based on the implicit representation model [19]. One benefit of developing this model is to inherently guarantee the connectivity between any two GMs. Moreover, the approach adopts a reduced-order model for calculating the effective properties of intermediate GMs by interpolating those of a set of key-GMs at given sampling points. This strategy is able to significantly reduce the computational cost for solving the downscale homogeneous equations, and thus improves computational and design efficiency.

Lattice cantilever beams comprised of varying GMs are optimized by using the proposed method. In addition, optimized UM beams with the same mass are also investigated for comparison. Both designs are fabricated by AM and their stiffness properties are experimentally determined. The simulation/experimental results show that the optimized GM beams clearly demonstrate their mechanical advantage in terms of improved stiffness compared to the UM baseline design.

## 2. Geometrical model

Conventional design methods typically incorporated UMs into CSs (see Fig. 1(a) and (b)), which is easy to be implemented but may prevent finding better-performing CSs. It is more advisable to allow for spatially-varying mesostructures when designing CSs, as illustrated in Fig. 1(c). In this section, we will develop a configuration interpolation model to construct a family of essentially connectable GMs of varied mechanical properties.

In the following illustrations, we make a convention for stating the geometrical and physical quantities at two length scales, in which the superscripts ‘gs’ and ‘ms’ indicate that the quantities are evaluated at the global-scale and meso(or local)-scale levels, respectively;  $\mathbf{x}$  and  $\mathbf{y}$  denote coordinate vectors of global and local points at two scale levels; and all the pictures make use of gray and color regions to represent GM layout and configurations.

### 2.1. Level set representation

In this study, the level set model is adopted to represent the configurations of lattice structures, because of its unique merits in terms of

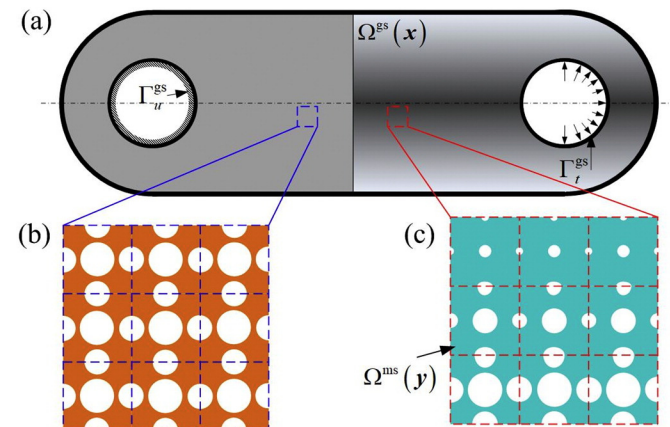


**Fig. 1.** (a) A bracket CS involving (b) uniform and (c) spatially-varying mesostructures, in which gray regions indicate layout patterns of the contained mesostructures, characterized by their relative densities, and color regions are used for separating UMs from GMs.

distinct interface identification, shape fidelity and topological flexibility. Moreover, the level set model can be easily fitted into the structural optimization framework, making rapid developments for designing novel engineering structures and seeking new artificial materials [32, 33].

The level set method specifies boundaries of macrostructure as zero-contours of a higher-order level set function (LSF), i.e.  $\Phi = 0$ , and then distinguishes solid regions by positives  $\Phi > 0$  and void regions by negatives  $\Phi < 0$ . The level set model used for representing local mesostructures is defined in a similar manner, denoted by  $\varphi(\mathbf{y})$ .

When considering dynamic movement of structural frontiers, a pseudo-time  $t$  is introduced into the LSFs, and then the configurations of global structures and local mesostructures can be respectively evolved by solving the following Hamilton-Jacobi equations,

$$\frac{\partial \Phi(\mathbf{x}, t)}{\partial t} - V_n |\nabla \Phi| = 0, \quad \frac{\partial \varphi(\mathbf{y}, t)}{\partial t} - v_n |\nabla \varphi| = 0 \quad (1)$$

where  $V_n$  and  $v_n$  are the corresponding normal velocities. Here, a second-order essential non-oscillatory finite differential scheme is used to solve Eq. (1) [33]. In general, both LSFs are initialized as signed distance functions, and re-initialized every 3 iterations during the course of the optimization process.

## 2.2. Configuration interpolation model

As mentioned in the introduction, disconnected neighboring mesostructures may be found in the optimal solutions in a decoupled design strategy, as illustrated in Fig. 2(a). Disconnected regions will lose their load bearing capability. A desirable design result should contain connected mesostructures, in which each member is taken as a part of the force transmission path, as shown in Fig. 2(b).

To address the issue, we develop a configuration interpolation model to construct a family of connectable GMs. The underlying concept of the method is to interpolate the LSFs of two end-frame cells to yield intermediate GMs. That is, provided two end-frame cells are represented by  $\varphi_1$  and  $\varphi_N$ , the configuration of any  $i$ th intermediate GM is characterized by,

$$\varphi_i(\mathbf{y}) = f_i \varphi_1(\mathbf{y}) + (1-f_i)(\varphi_1 - \min(\varphi_1)) = 0 \quad (2)$$

with the interpolation defined by,

$$f_i = f(\alpha_i) = (1-\alpha_i^p)^{1/p}, \quad 0 \leq \alpha_i \leq 1 \quad (3)$$

where  $\alpha_i$  is an interpolation parameter and  $p$  is the penalty factor. It is worth noting that Eq. (2) can reproduce fully-solid GM, with non-negative values throughout the entire cell domain.

It is found that the obtained GMs are dependent on  $\varphi_1$ , and therefore it is important to optimize a basic mesostructure characterized by  $\varphi_1$  for generating other GMs. Different from microstructured material design, the basic mesostructure should be designed as a load-bearing component and its configuration should be determined regarding to the global

structural configuration and the given load condition (see the given example in Sections 4 and 5).

It is seen from Eq. (2) that each interpolated GM is actually constructed by extracting an intermediate slice between the zero contour (i.e.  $\varphi_1 = 0$ ) and solid layers of a unique characteristic LSF, as illustrated in Fig. 3. This process is equivalent to taking the GM as the solid part that is enclosed by iso-contours with a constant distance to the structural boundaries. In this sense, all the GMs offer similar topological features, especially on their corresponding surfaces. Hence, they can be inherently connected with each other. Moreover, the construction process is implemented without prior knowledge of the basic mesostructure configuration, and thus it allows for interpolation of any shapes without explicit geometric parameters. In addition, the construction process allows for topological changes for the obtained GMs.

The relative density of the  $i$ th GM is defined as the volume ratio occupied by the base materials over the cell domain, calculated by,

$$\rho_i = \frac{1}{V^{\text{ms}}} \int_{\Omega_i^{\text{ms}}} d\Omega \quad (4)$$

Since the configuration interpolation process is actually to thicken member parts, the relative density of the  $i$ th GM satisfies  $\rho_1 \leq \rho_i \leq \rho_N$ , which can be checked through Eqs. (2) and (4).

Although the obtained GMs can be naturally connected, mismatched material distributions at the common edges may be found. To tackle this issue, we apply a filtering strategy on the GMs layout design process to control the global variation of the GMs. This is followed by a global smoothing step during post-processing to alleviate any mismatched connections.

## 3. Mechanical model

When simulating the mechanical behavior of a lattice structure by using the finite element method, it is impossible to incorporate all the details of local mesostructures into system equations, because of the huge number of degrees of freedom for the fine-scale model. In order to handle this issue, we carry out a multiscale finite element method for calculating the mechanical response of the lattice structures. Moreover, we developed a reduced-order model to efficiently estimate the homogenized elasticity tensors of intermediate GMs. In the following,  $\mathbf{u}(\mathbf{x})$  and  $\chi(\mathbf{y})$  denote displacement at a global  $\mathbf{x}$  and a local  $\mathbf{y}$  points, respectively; and  $\boldsymbol{\varepsilon}(\mathbf{u})$  and  $\boldsymbol{\varepsilon}(\chi)$  are the strain tensors induced by the corresponding displacement fields.

### 3.1. State equations

In the framework of linear elasticity, deformation of a solid body at its equilibrium state can be calculated by solving the following equation,

$$\int_{\Omega^{\text{gs}}} \boldsymbol{\varepsilon}(\mathbf{u}) : \mathbf{D}(\mathbf{x}) : \boldsymbol{\varepsilon}(\mathbf{v}) d\Omega = \int_{\Gamma_t^{\text{gs}}} \mathbf{t} \cdot \mathbf{v} d\Gamma + \int_{\Omega^{\text{gs}}} \mathbf{b} \cdot \mathbf{v} d\Omega, \quad \mathbf{v} \in U_{\text{ad}} \quad (5)$$

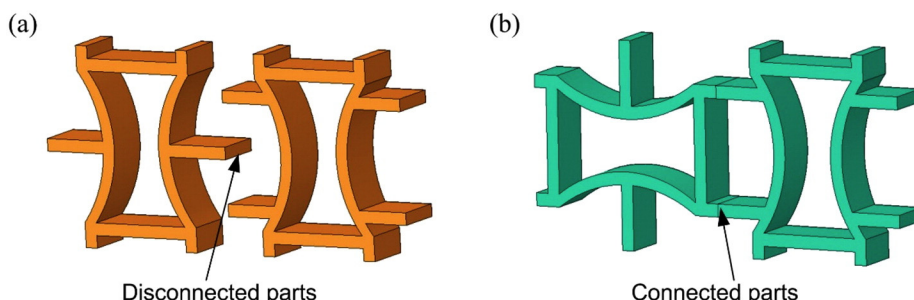
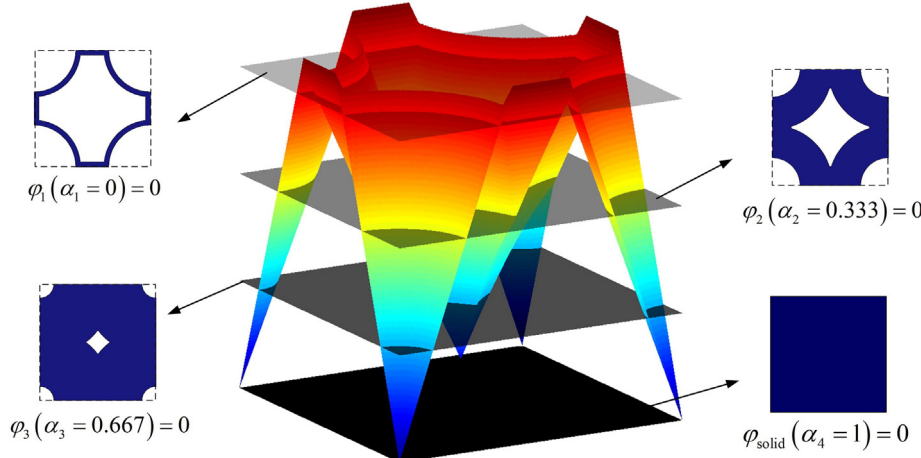


Fig. 2. Two neighboring cells involving (a) disconnected and (b) connected parts.



**Fig. 3.** Schematic illustration of the construction process of connectable GMs, where each GM is obtained by extracting zero-counters of different layers of a unique characteristic LSF.

where  $\mathbf{v}$  is virtual displacement field belong to kinetically admissible space  $U_{ad}$ ;  $\mathbf{t}$  and  $\mathbf{b}$  are the traction and body force; and  $\mathbf{D}(\mathbf{x})$  is the elasticity tensor at point  $\mathbf{x}$ .

When the body is comprised of local mesostructures, the mechanical properties of a point within the mesostructure regions are evaluated by the effective average of local property variations at the downscale level. Here, the asymptotic homogenization method [15] is used to calculate the effective properties at point  $\mathbf{x}$  by,

$$\mathbf{D}(\mathbf{x}) = \mathbf{D}^H(\mathbf{x}) = \frac{1}{V^{ms}} \int_{\Omega^{ms}} (\boldsymbol{\epsilon}^0 - \boldsymbol{\epsilon}(\chi)) : \mathbf{D}^s : (\boldsymbol{\epsilon}^0 - \boldsymbol{\epsilon}(\chi)) d\Omega \quad (6)$$

where  $\mathbf{D}^s$  is the elasticity tensor for the basic constituent material;  $V^{ms}$  is the volume of the whole cell domain;  $\boldsymbol{\epsilon}^0$  is the induced unit strain field to be applied at the cell domain  $\Omega^{ms}$ ; and the local displacement field  $\chi$  can thus be obtained by solving the homogenous equation,

$$\int_{\Omega_i^{ss}} (\boldsymbol{\epsilon}^0 - \boldsymbol{\epsilon}(\chi)) : \mathbf{D}^s : \boldsymbol{\epsilon}(\zeta) d\Omega = 0, \quad \forall \zeta \in \bar{U}_{ad} \quad (7)$$

where  $\zeta$  is the virtual displacement that is contained in the kinetically admissible space  $\bar{U}_{ad}$ . In general, the periodic condition is imposed when solving Eq. (7), resulting in a continuous material distribution on the opposite surfaces. To this end, the deformation of a CS can be obtained by substituting Eqs. (6) and (7) into Eq. (5).

The homogenization Eqs. (6) and (7) have been widely used for compliance minimization of lattice structures, even for the cases with spatially-varying microstructures [5, 10, 17]. They can effectively capture stiffness variation of the lattice structure with respect to changes of microstructural configurations as well as lattice layout patterns. Hence, they can be used for finding reasonable optimized solutions. It will be seen that the homogenization method works quite well for our design approach, in which improvement of structural stiffness for numerical and experimental results are quite close. If more accurate solutions are expected, for instance to calculate local stress distribution, advanced multiscale finite element methods might be preferable.

### 3.2. Reduced-order property interpolation

It is computationally expensive to directly calculate the homogenized properties of all the intermediate GMs over the entire space of  $0 \leq \alpha_i \leq 1$ . In order to improve the computational efficiency, we develop a more economic property estimation strategy in a reduced-order manner. Here, we first conduct the computations of Eqs. (4) and (6) at a finite number of key points at  $\alpha_k = (k-1)/N$ ; and then, for any

intermediate GM provided a relative density  $\rho_e$ , its homogenized elasticity tensor can be linearly interpolated by,

$$\mathbf{D}_e^H = \frac{\rho_{k+1} - \rho_e}{\rho_{k+1} - \rho_k} \mathbf{D}_k^H + \frac{\rho_e - \rho_k}{\rho_{k+1} - \rho_k} \mathbf{D}_{k+1}^H, \quad (k = 1, 2, \dots, N-1) \quad (8)$$

on the condition satisfying  $\rho_k \leq \rho_e \leq \rho_{k+1}$ , where  $N$  is the total number of specific key-GMs; and the elasticity tensor  $\mathbf{D}_k^H$  of the  $k$ th key-GM is calculated by Eqs. (6) and (7).

Obviously, the interpolation accuracy of Eq. (8) is dependent on the number of the key-GMs used, in which higher accuracy can be expected by more key-GMs. However, with a large number of key-GMs, the computational cost would be extremely high by solving linear equations of Eq. (7) for each key-GM. By balancing the computational accuracy and efficiency, we set 18 key-GMs when solving the following optimization problem.

### 3.3. Region indicator

CSs are always comprised of low relative density mesostructures. To prevent designed CSs from buckling [34], an additional solid layer is attached to the structural boundary, with a uniform thickness  $h$ , as shown in Fig. 4. The solid layer can be exactly modeled as a point set of  $\{\mathbf{x} | \Phi(\mathbf{x}) > 0 \& \Phi(\mathbf{x}) - h < 0\}$ . The value of  $h$  does play an important role on influencing the mechanical performance of optimized solutions, and a comprehensive discussion on this issue is referred to [35]. In the numerical study,  $h$  is set to be 0.2 times the size of the elements for analysis.

In order to determine the region that a computational point  $\mathbf{x}$  is positioned in, an indicator is defined by,

$$Ind(\mathbf{x}) = H(\Phi) + H(\Phi - h) \quad (9)$$

where  $H(\bullet)$  is the Heaviside function; point  $\mathbf{x}$  is marked to be in the void region if  $Ind(\mathbf{x}) = 0$ , in the solid layer region if  $Ind(\mathbf{x}) = 1$  and in the cell region if  $Ind(\mathbf{x}) = 2$  (see Fig. 4).

In the numerical computation, finite elements may be intersected by structural boundaries and solid layers. In this regard, an Ersatz model is used to solve the global equilibrium Eq. (5). That is, a set of computational points is set for numerical integration; the elasticity tensor  $\mathbf{D}(\mathbf{x})$  at a computational point  $\mathbf{x}$  can then be evaluated by  $\mathbf{D}^v$ ,  $\mathbf{D}^s$  and  $\mathbf{D}^H$  if it locates in void, solid layer and cell regions, respectively, as shown in Fig. 4. Here,  $\mathbf{D}^v = 10^{-8} \mathbf{D}^s$  is an artificial weak material to prevent numerical singularity when solving Eq. (5). It has been reported that this model is quite effective and efficient for a stiffness optimization problem [31, 32].

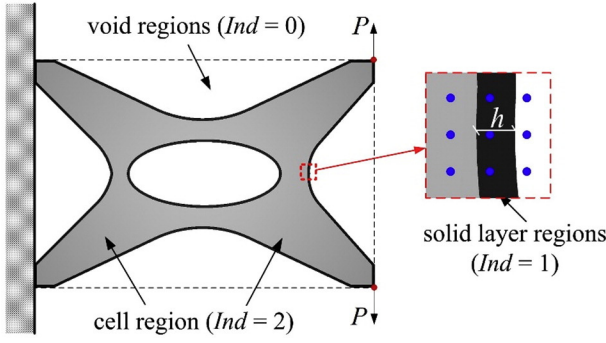


**Fig. 4.** Schematic illustration for indicators of various regions, in which an additional solid layer of thickness  $h$  is attached to structural boundaries for preventing buckling. The blue circular points stand for computational points within an element.

#### 4. Optimization model

Mechanical CSs with GMs are optimized to have superior structural stiffness, in comparison to baseline designs with UMs. Making use of the above developed configuration interpolation and reduced-order computation models, the compliance minimization problem for the CSs with GMs can be formulated by,

$$\begin{aligned} \min_{\Theta} \quad & J(\Theta) = \int_{\Omega^{\text{gs}}} \boldsymbol{\varepsilon}(\mathbf{u}) : \mathbf{D}(\mathbf{x}) : \boldsymbol{\varepsilon}(\mathbf{u}) d\Omega \\ \text{s.t.} \quad & a(\mathbf{u}, \mathbf{v}, \Theta) = l(\mathbf{v}, \Theta), \quad \forall \mathbf{v} \in U_{\text{ad}} \\ & G_{\text{vol}} \leq 0 \end{aligned} \quad (10)$$

where  $J(\Theta)$  is the cost function, i.e. the overall compliance of the structure;  $\Theta$  indicates various types of design variables, and  $G_{\text{vol}}$  is the volume constraint; the equilibrium equation(s) is expressed in its equivalent integral form, where the bilinear energy  $a(\mathbf{u}, \mathbf{v}, \Theta)$  and the linear load  $l(\mathbf{v}, \Theta)$  can be obtained from Eqs. (5) and (7).

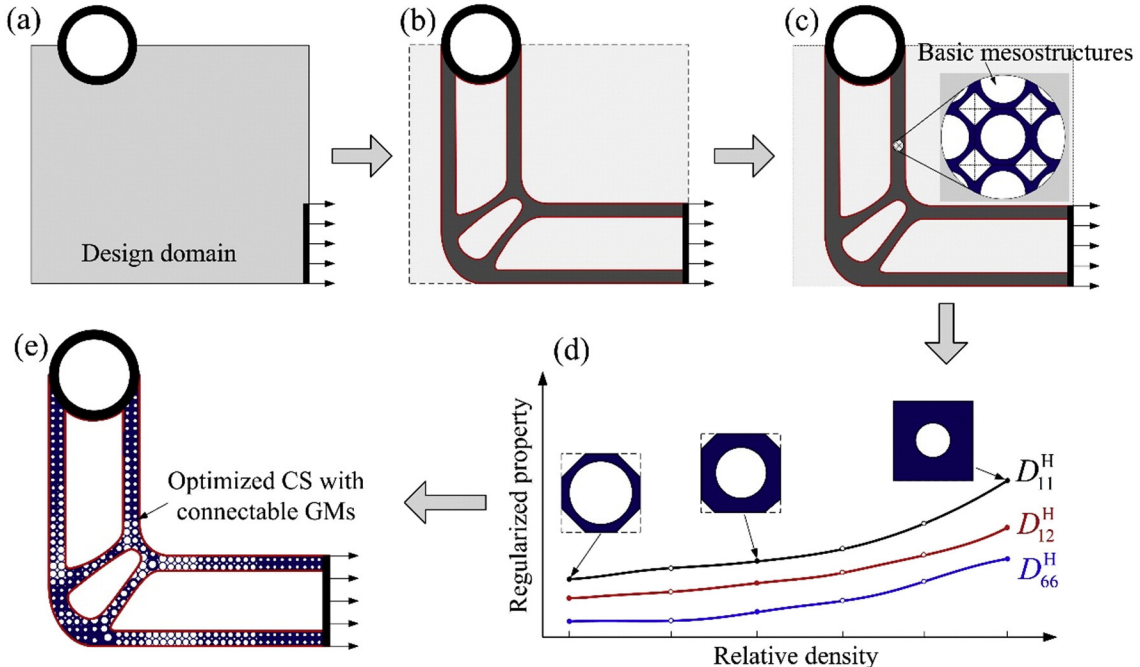


**Fig. 5.** Schematic illustration of multiscale CS design process. (a) Design domain; (b) optimized global structure; (c) CS comprised of optimized basic mesostructures; (d) interpolated GMs with their effective elasticity tensors versus relative densities; and (e) final optimized CS with spatially-varying GMs.

#### 4.1. Optimization flowchart

In the proposed multiscale CS design framework, problem (10) is solved in a subsequent design process. The global structural geometry, GM configurations and their layout pattern will be optimized by carrying out a three-step optimization at different length scales, as illustrated in Fig. 5. For each optimization process, different types of design variables and volume constraints are defined, and thus various optimization algorithms are correspondingly adopted.

- *Step-1 Structural configuration optimization:* a primary optimized global structure is determined (see Fig. 5(a) to (b)), where the ‘solid’ region is filled by an isotropic material. Therein, the global structural geometry is taken as the design variable  $\Theta = \Phi$ , and the volume constraint is given to restrict the percentage of the isotropic material by,

$$G_{\text{vol}}^{\text{gs}} = \int_{\Omega^{\text{gs}}} d\Omega - f_{\text{gs}} V^{\text{gs}} \quad (11)$$

where  $f_{\text{gs}}$  is the allowable fraction of the areas covered by the potential GMs, which is always freely defined by the users or according to the real requirement in real engineering problems, and  $V^{\text{gs}}$  is the volume of the global design domain. To represent the mechanical properties of the material, it reads  $\mathbf{D}(\mathbf{x}) = \mathbf{D}^s$  when solving Eq. (5).

- *Step-2 Basic mesostructure optimization:* the basic mesostructure is optimized to be uniformly substituted into the ‘solid’ regions of the optimized global structure in Step-1 (see Fig. 5(b) to (c)), and thus the configuration of the basic mesostructure is taken as the design variable, i.e.  $\Theta = \varphi_1$ . The volume constraint here is imposed to restrict the usage of the base materials within the cell domain  $D^{\text{ms}}$  by,

$$G_{\text{vol}}^{\text{ms}} = \int_{\Omega^{\text{ms}}} d\Omega - f_{\text{ms}} V^{\text{ms}} \quad (12)$$

where  $f_{\text{ms}}$  is the given volume ratio of the base material of the designed basic mesostructure. Then, a family of GMs are constructed from the optimized basic mesostructure by using the configuration interpolation model developed in Section 2.2. Their homogenized

properties and relative densities are calculated according to Eqs. (6) and (4) (in Fig. 5(d)).

It is found from Eq. (4) that the relative density of the basic mesostructure indicates the lower bound of all the interpolated GMs. Hence, the volume ratio  $f_{\text{ms}}$  in Eq. (12) should be set to be as small as possible for a sufficient large design space. However, designing a basic mesostructure of small volume ratio typically means small member features and higher computationally cost. A tradeoff between performance and computational efficiency should be determined for prescribing  $f_{\text{ms}}$ .

- *Step-3 GMs layout optimization:* after construction of the GMs, the final step is to seek their best layout pattern (see Fig. 5(d) to (e)). Here, the relative densities of the macro-elements  $\rho_e$  are taken as the design variables, i.e.  $\Theta = \rho_e$ , which determines the GM candidate to be attached into the element. The effective properties at a computational point within the element are obtained by Eqs. (6) to (8).

As for most topology optimization methods, a density bound condition is imposed by.

$$\rho_{\min} \leq \rho_e \leq \rho_{\max} \quad (13)$$

where  $\rho_{\min}$  and  $\rho_{\max}$  are the corresponding minimum and maximum density variable thresholds. To avoid internal members becoming detached, it should also satisfy  $f_{\text{ms}} \leq \rho_{\min}$ . The volume constraint is to restrict the total volume ratio of the base material in the designed CS, given by,

$$G_{\text{vol}}^{\text{cs}} = \sum_{e=1}^{N_e} \rho_e V_e - f_{\text{cs}} V^{\text{gs}} \quad (14)$$

where the subscript 'cs' stands for the cellular structure;  $N_e$  is the number of the elements at the global scale level;  $V_e$  is the volume of the eth element and  $f_{\text{cs}}$  is the volume ratio of the base material of the entire CS after the whole design.

#### 4.2. Sensitivity analysis

It is noted that different types of design variables are utilized in the three-step optimizations: in the first two steps, the topological configuration of either the global structure or the basic mesostructure is evolved by solving the Hamilton-Jacobi equations (1); and the last optimization process updates the element-wise densities by using the 'method of moving asymptotes' optimizer [36]. All algorithms are implemented based on the derivative of the cost and constraint functions with respect to each type of design variables. Hence, (shape) sensitivity analysis should be carried out.

The augmented Lagrangian function of the design problem (10) can be formulated by,

$$\mathcal{L} = J(\Theta) - \lambda G_{\text{vol}} + \frac{1}{2} \mu G_{\text{vol}}^2 \quad (15)$$

where  $\lambda$  and  $\mu$  are the Lagrange multiplier and the penalty factor, respectively. It is known that the optimization problem (10) is actually self-adjoint. In this sense, the material derivative of the cost function in the structural configuration optimization step yields:

$$\frac{d\mathcal{L}}{dt} = - \int_{\Gamma^{\text{gs}}} [\boldsymbol{\varepsilon}(\mathbf{u}) : \mathbf{D}^s : \boldsymbol{\varepsilon}(\mathbf{u}) + (\lambda^{\text{gs}} - \mu G_{\text{vol}}^{\text{gs}})] V_n d\Gamma \quad (16)$$

To guarantee a feasible descending direction, i.e.  $d\mathcal{L}/dt$ , the normal velocity can be selected by,

$$V_n(\mathbf{x}) = \boldsymbol{\varepsilon}(\mathbf{u}) : \mathbf{D}^s : \boldsymbol{\varepsilon}(\mathbf{u}) + \lambda^{\text{gs}} - \mu G_{\text{vol}}^{\text{gs}}, \quad \forall \mathbf{x} \in \Gamma^{\text{gs}} \quad (17)$$

A similar derivative result as Eq. (16) can be obtained for the basic mesostructure optimization process, where the normal velocity on the boundary is selected by,

$$v_n(\mathbf{y}) = \int_{\Omega_e^{\text{gs}}} \boldsymbol{\varepsilon}(\mathbf{u}) : [(\boldsymbol{\varepsilon}^0 - \boldsymbol{\varepsilon}(\chi)) : \mathbf{D}^s : (\boldsymbol{\varepsilon}^0 - \boldsymbol{\varepsilon}(\chi))]_y \\ : \boldsymbol{\varepsilon}(\mathbf{u}) d\Omega + \lambda^{\text{ms}} - \mu^{\text{ms}} G_{\text{vol}}^{\text{ms}}, \quad \forall \mathbf{y} \in \Gamma^{\text{ms}} \quad (18)$$

where  $[\square]_y$  denotes that all the internal terms are evaluated at point  $\mathbf{y}$ . Since the velocities in Eqs. (17) and (18) are defined on the structural boundaries, a natural extension strategy [32] is used to extend them into the entire design domain for solving the Hamilton-Jacobi equations.

At the GMs layout optimization step, the first-order derivative of the cost function with respect to the discrete design variable  $\rho_e$  is calculated by,

$$\frac{\partial J}{\partial \rho_e} = - \int_{\Omega_e^{\text{gs}}} \boldsymbol{\varepsilon}(\mathbf{u}) : \tilde{\mathbf{D}} : \boldsymbol{\varepsilon}(\mathbf{u}) d\Omega, \quad e = 1, 2, \dots, N_e \quad (19)$$

where  $\Omega_e^{\text{gs}}$  is the region occupied by the eth element at the global scale, and tensor  $\tilde{\mathbf{D}}$  is given depending on the indicator  $Ind(\mathbf{x})$ . It should be noted that Eq. (8) provides a non-smooth interpolated property curve for the obtained GMs, and therefore a forward finite difference scheme is used to calculate the derivatives of the elasticity tensor with respect to densities. In this regard, it has,

$$\tilde{\mathbf{D}}(\mathbf{x}) = \begin{cases} \mathbf{D}^v, & \text{if } Ind(\mathbf{x}) = 0 \\ \mathbf{D}^s, & \text{if } Ind(\mathbf{x}) = 1 \\ (\mathbf{D}_{k+1}^H - \mathbf{D}_k^H) / (\rho_{k+1} - \rho_k), & \text{if } Ind(\mathbf{x}) = 2 \end{cases} \quad (20)$$

The derivative of the volume constraint is written by,

$$\frac{\partial G_{\text{vol}}^{\text{cs}}}{\partial \rho_e} = V_e, \quad e = 1, 2, \dots, N_e \quad (21)$$

#### 4.3. Discussion

It is noted that a multi-step flow is presented in Fig. 5. In order to test its performance, a three-point bending problem under fully-fixed boundary conditions at two lower corners is solved. Geometric, optimization parameters and loading conditions are shown in Fig. 6(a). For comparison, both optimized lattice beams consisting of UMs and GMs are presented in Fig. 6(b) and (c), respectively. Additionally, an extended design strategy was performed by looping the first two steps in an integrated manner, where the 'solid' parts in Fig. 5(b) were assigned by the mechanical property of the optimized mesostructure from Fig. 5(c). The corresponding optimized solution for the integrated design is given in Fig. 6(d). The optimized compliances for all the cases are listed in the figure caption.

From the results, an obvious stiffness improvement can be found for the optimized GM beams compared to the UM beam. Here, the configuration interpolation technology constructs a set of connectable GMs of various mechanical properties, therefore greatly expanding the design space. However, since the optimized GMs are all belonging to a certain set of topologies, the final solutions could be compromised. Two technologies can be developed to improve the performance of the obtained solutions. One is to apply for more types of interpolation functions, for instance by sine-type series, for Eq. (2), which is able to expand the design space of GM candidates for the GM layout process. The other method is to additionally optimize GM orientations at each global point [37], aligning their member parts with principle strain directions. Both strategies can provide improved designs to at least a certain extent.

By comparing the results in (c) and (d), it is found that the multi-step and integrated design strategies generate solutions of similar compliances for this specific problem. This result illustrates that the design

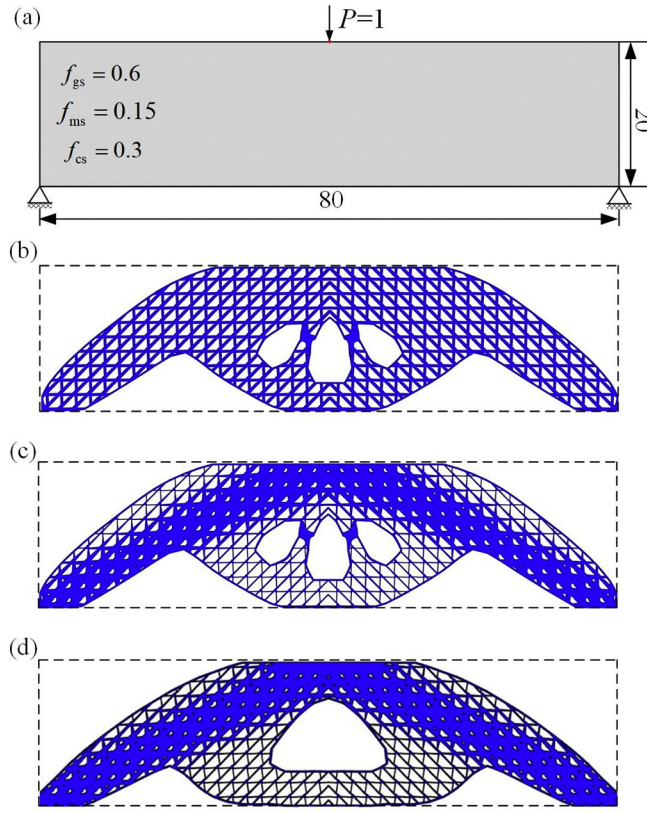


**Fig. 6.** Optimization of three-point bending beams. (a) Design domain, (b) optimized UM beam with  $J^{\text{opt}} = 106.81$ , (c) optimized GM beam with  $J^{\text{opt}} = 64.67$ , (d) optimized GM beam using an integrated design strategy with  $J^{\text{opt}} = 64.14$ .

flow in Fig. 5 can provide designers satisfied solutions for engineering applications. The numerical technologies developed in this study, such as configuration interpolation and reduced-order computation, can be used for an integrated or concurrent design framework, but the implementation may call for additional numerical efforts and would typically lead to dramatic increase on computing time.

## 5. Numerical study

The compliance minimization problem of a cellular cantilever beam is solved by using the proposed approach. Here, a rectangular beam comprised of  $20 \times 15$  unit cells with a uniform unit thickness is considered under the plane stress framework. The beam is clamped at the left side and loaded by a unit upward concentrated force at the top-right corner. A fictitious linear isotropic base material is assumed, with dimensionless Young's modulus  $E^s = 1$  and Poisson's ratio  $\mu = 0.3$ . All three optimization steps are terminated under the condition that the relative difference of the cost functions between the two subsequent iterations is lower than  $10^{-4}$ . A set of  $40 \times 30$  unit-sized quadrilateral four-node square elements are used to discretize the beam, where each cell containing  $2 \times 2$  elements is attached to a potential GM candidate.

For comparison, optimizations are performed for the beams involving both UMs and GMs. When interpolating properties of intermediate GMs, a total number of 18 key-GMs are used. The volume fractions in Eqs. (11), (12) and (14) are set to be  $f_{\text{gs}} = 0.5$ ,  $f_{\text{ms}} = 0.15$  and  $f_{\text{cs}} = 0.25$ , respectively, which means that the final volume ratio of the optimized results is identically restricted to be 25% of the entire design domain. In order to investigate the influence of various ranges of GMs, we define four cases of different  $\rho_{\min}$  and  $\rho_{\max}$  in Eq. (13) for the GMs layout optimization process, as per parameters given in Table 1. Here, the optimized solution of case 1 represents the case of optimized UM beam

since the upper and lower bounds are close to each other. The mechanical advantages of GM designs are measured by  $\eta = |J_{\text{GM}}^{\text{opt}} - J_{\text{UM}}^{\text{opt}}|/J_{\text{UM}}^{\text{opt}}$ .

Fig. 7 presents the optimized GMs as well as their elasticity tensors versus relative densities. Here, 'regularized' means that the homogenized properties of the GMs are normalized by  $E/(1 - \mu^2)$ . It is seen that the optimized GMs present 2D Kagome-like configurations, composed of two intersected beams between external solid panels. However, instead of uniform-sized beams in the conventional Kagome structures, the optimized GMs exhibit anisotropic behavior with relatively thicker beams directing to the load point. Therefore, the optimized GMs are capable of offering a high directional stiffness to resist the bending deformation, further enhancing their load-bearing capabilities. Fig. 8 presents optimized UM and GM beams of cases 1 and 2, respectively, in which the optimized beams are comprised of optimized mesostructures in Fig. 7(a). It can be found from the results that making use of the developed configuration interpolation technology is able to guarantee the connectivity of the GMs in the optimized solutions, preventing impending and disconnected parts. Table 1 presents the final compliances of the optimized cellular beams. It is observed that the optimized GM beams have significantly improved global stiffness compared to the optimized UM beam. Moreover, including a wider density and stiffness span of GMs results in higher stiffness. The results clearly illustrate the advantages of the design process with spatially varying GMs. However, the optimized GMs with low densities typically contain small member width, which cannot be printed by commercially available 3D printers (see Fig. 7(a)). In order to handle this issue, we increase  $\rho_{\min}$  to control the minimum width in the optimized CSs. This is due to the fact that the GMs of higher relative densities typically involve thicker member parts. Finally, case 2 (in Fig. 8(b)) was selected to be printed and tested. An alternative design strategy to control the minimum width is to impose a size constraint when designing the basic mesostructure (referred to [38–40]).

## 6. Experimental validation

### 6.1. AM process

Both the optimized UM and GM beams in Fig. 8 are additively manufactured with MultiJet printing technology using a ProJet 5500X printer. Droplets of photo-sensitive liquid resin are selectively deposited onto a substrate through a movable nozzle, and simultaneously solidified through ultraviolet light. We choose this printer mainly because it enables the printing of a large-sized part to a high resolution. The printable minimal feature size of the specimens is approximately 0.3 mm, but removal of wax supports from small holes becomes quite difficult. A minimum width of 0.6 mm was set for the optimized beam in Fig. 8(b).

An ABS-like material, Visijet CR-WT is selected as the base material. In-house ASTM D638 standard tensile tests indicate that the tensile response is almost independent of printing direction and lattice diameter (within accurate printing resolution). The tensile and compressive stiffness is close for small strain values. Fig. 9 shows a representative tensile stress-strain curve of this material. The material does not display an ideal linear elastic region; instead, the stiffness gradually decreases with increase of stress. Herein, the Young's modulus in the stress range of 2–10 MPa is determined as 2.0 GPa.

**Table 1**

Thresholds of densities for the GMs distribution design for different cases, corresponding optimized cost function values.

Case	$\rho_{\min}$	$\rho_{\max}$	$J^{\text{opt}}$	$\eta(\%)$
1	0.495	0.505	822.24	NA
2	0.300	0.950	623.55	24.16
3	0.200	0.950	573.84	30.21
4	0.150	0.950	554.53	32.56

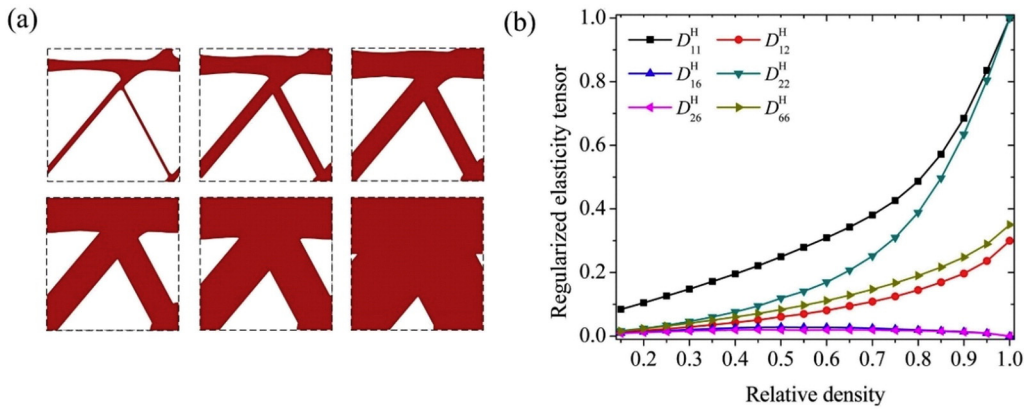


**Fig. 7.** (a) Optimized GMs together with (b) interpolated curves of their elasticity tensors.

Before printing, 3D geometric models for both types of beams are generated. Here, exact planar geometries of the optimized beams can be built from the corresponding implicit LSF by using the marching square algorithm. Solid 3D models are created by extruding the obtained 2D geometries along the out-of-plane direction, e.g. using CAD software such as SolidWorks. The designed beams are 160 mm in length by 120 mm in width and 15 mm in thickness. The thickness of the additional solid layer is about  $h = 0.8$  mm. Additional 6 mm diameter bolted connections are included in the solid model to achieve a clamped boundary condition. A 4 mm diameter hole is also included at the end of the cantilever beam for load application. Finally, STL files are generated for 3D printing. For any interested readers, we can provide the STL files of the uniform and optimized lattice beams upon request.

For each type of the optimized beams, we printed three specimens. Fig. 10 presents one of the printed samples for both the UM and GM beams, with similar masses of  $117.0 \pm 1.2$  g and  $117.8 \pm 0.2$  g, respectively. The slight deviation is due to the manufacturing variation and the residual wax. The wax support material is required during the printing process and removed by melting after printing.

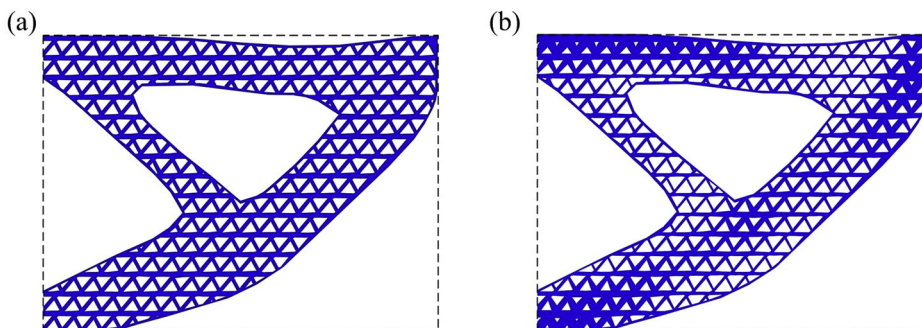
## 6.2. Mechanical test

Experimental validation was carried out for the two designs shown in Fig. 10. The experiments were conducted on an Instron 5982 universal test machine with a 1.0 kN load cell, according to the experimental setup shown in Fig. 11. All of the specimens were loaded by lifting the top-right bracket upwards at a speed of 0.5 mm/min, which is to simulate the quasi-static condition. Each test was stopped at a maximum displacement of 4.0 mm. A linear variable differential transformer (LVDT) was attached to the end of the clamped fixture in order to monitor the fixture's vertical deflection.

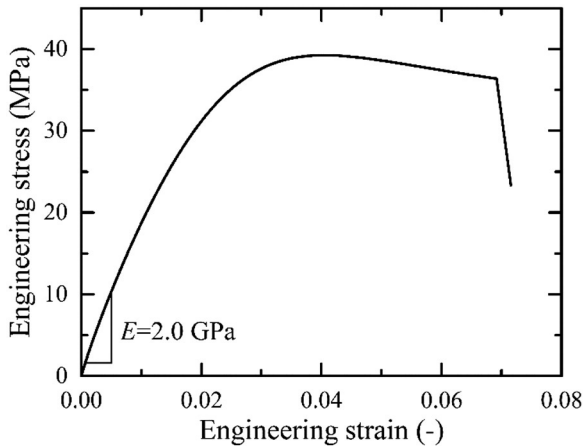
## 6.3. Results and discussions

Fig. 12 shows the measured load–displacement responses of the specimens, together with the deviation error analysis (see shading regions). It is observed that all samples remained in-plane during the loading process. The maximum deflection of the fixture recorded by the LVDT was below 0.08 mm, which is small compared to that of the tested lattice beams and can therefore be neglected. Since the samples were only tested for stiffness validation within the linear elastic region as well as under the geometrical linearity condition for small displacements, the curves within the load range between 150 N to 250 N are used to evaluate the stiffness of the samples. The global stiffness of the specimens is evaluated by linear regression, with resulting values of  $S_{\text{UM}} = (1.7 \pm 0.1) \times 10^2$  N/mm and  $S_{\text{GM}} = (2.1 \pm 0.1) \times 10^2$  N/mm for the UM and GM beams, respectively. The standard deviations of the stiffness for both types of beams are below 6.1%, which illustrates the repeatability of the experiments. The measured stiffness values clearly demonstrate the superior stiffness of the GM beams over the UM beams, with a significant improved global stiffness of 23.6%. It should be noted that the tested beams showed smooth stiffness decreases with an increase in applied load, similar as depicted in the material stress–strain curve in Fig. 9. This material nonlinearity can lead to variations in stiffness evaluation and the discrepancy of the stiffness improvement between testing and simulation. In addition, small differences in boundary conditions could contribute to the discrepancy that the left sides of the beams are rigidly fixed for all the degrees of freedoms in the optimization process, while they are relaxed by an elastic boundary condition for the tested samples.

Here, experiments were conducted only for testing stiffness of optimized lattice beams, which is in general a standard requirement for most engineering applications. On the other hand, studying the influence of optimization on the ultimate strength of lattice structures is of great importance. However, incorporating stress or buckling constraints



**Fig. 8.** Optimized beams comprised of (a) UMs (for case 1) and (b) GMs (for case 2).



**Fig. 9.** Tensile stress–strain curve for Visijet CR-WT.

into optimization may cause various issues, such as convergence difficulty or buckling modal multiplicity, amongst others. A large number of studies in the optimization field have been made to address these issues for the one-scale structure optimization, e.g. [41–43], but limited papers can be found for lattice structure optimization with stress or buckling constraints. Studying the influence of the cell variation on the strength of optimized lattice structures will be part of our future work.

## 7. Conclusions and future work

In this paper, we proposed an effective design framework for designing graded lattice structures for AM, by linking the optimization steps of the global structural topology, the basic mesostructural configuration and the GMs layout pattern. Here, the connectivity of two neighboring GMs is guaranteed by developing an advanced configuration interpolation technology. In addition, a reduced-order model is developed to effectively and efficiently evaluate the properties of the interpolated GMs. Two cantilever beams involving UMs and GMs are optimized, additively manufactured and experimentally tested. Both the optimization and experimental results demonstrate the benefits of performing the multiscale structural design by using the proposed method. In addition, an important conclusion can be made that the optimized CS involving GMs is able to provide a higher stiffness than the UM design.

In numerical, there is no difficulty to extend the present method for designing 3D graded lattice structures, since all the techniques used in the approach (i.e. the level set representation model, numerical homogenization method and configuration interpolation) impose no restrictions on the problem dimensions. However, fabricating 3D optimized lattice structures may encounter issues such as removal of additional supports on the samples. Removing support structures may lead to structural distortion, which could significantly influence the mechanical

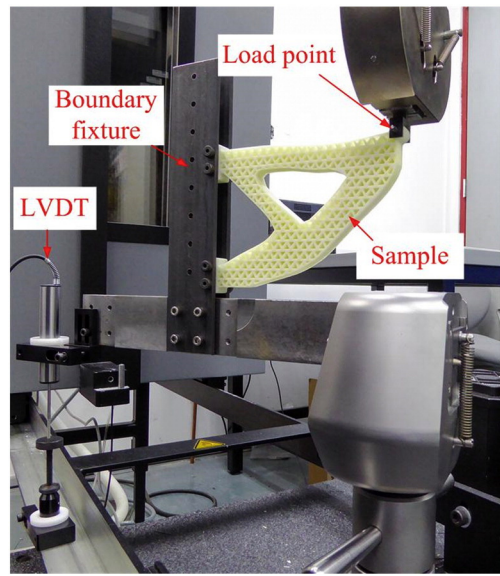


**Fig. 11.** Experimental setup.

performance of the samples. This issue could be addressed by optimizing process parameters or developing support-free 3D printing techniques.

One interesting topic is to compare the optimized CSs with GMs with the design from single-scale optimization with fully solid materials. According to the classical Michell's frame structural theory [44], GMs composed of two orthogonal beams along the principle strain directions would yield the optimal solutions. However, this conclusion can be made only at the infinitesimal local volume fractions [45]. Furthermore, the dimensional scales of the mesostructures compared to the global structure also have significant impact on the design solutions. A more comprehensive study for comparison will be conducted shortly.

Some other further works will be carried out to optimize the GMs composed of multiple materials in consideration of interface behavior for AM [46]. Another potential extension is to design the load-bearing conformal lattices aligned to the structural boundaries. In this context, a more accurate multiscale analysis method needs to be developed.

## Acknowledgements

The SIMTech authors, S. Feih and S. Daynes, acknowledge the support from the Agency for the Science Technology and Research and the Science and Engineering Research Council of Singapore through the Additive Manufacturing Centre Initiative (SERC Grant no. 142 68 00088). The authors acknowledge Mr. Lim Soon Cheong from the Department of Mechanical Engineering, National University of Singapore

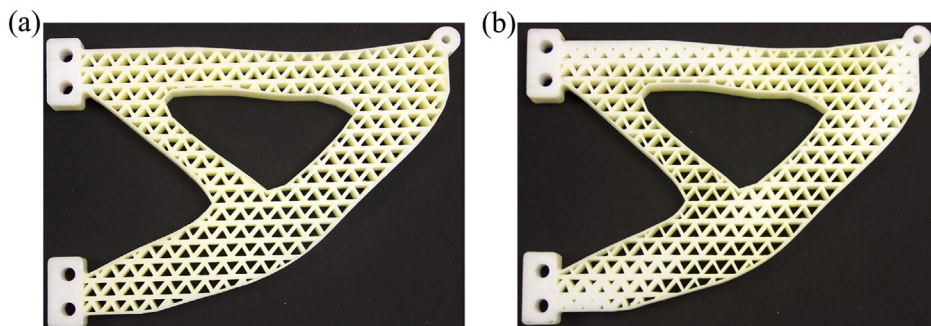


**Fig. 10.** 3D printed samples of (a) the UM beam and (b) the GM beam.

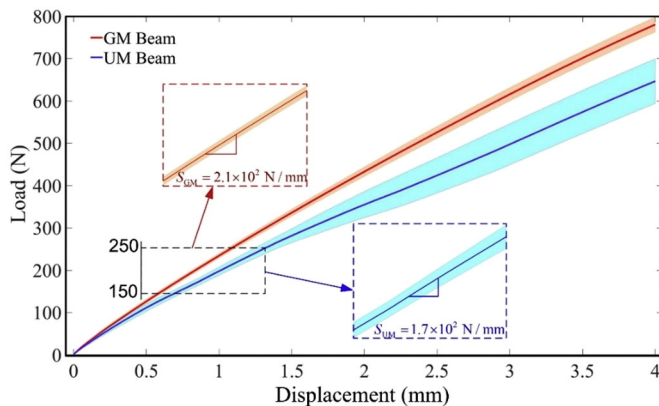


**Fig. 12.** Load-displacement curves for experimental verifications of UM (blue lines) and GM (red lines) beams, where shading regions indicate deviation analysis.

for manufacturing the testing fixtures, and SIMTech staff member Mr. Hengky Eng for 3D printing of the tested structures.

## References

- [1] L. Valdevit, A.J. Jacobsen, J.R. Greer, W.B. Carter, Protocols for the optimal design of multi-functional cellular structures: from hypersonics to micro-architected materials, *J. Am. Ceram. Soc.* (2011) 1–20.
- [2] J. Xiong, R. Mines, R. Ghosh, A. Vaziri, L. Ma, A. Ohrndorf, H.J. Christ, L. Wu, Advanced micro-lattice materials, *Adv. Eng. Mater.* 17 (9) (2015) 1253–1264.
- [3] V.S. Deshpande, N.A. Fleck, M.F. Ashby, Effective properties of the octet-truss lattice material, *J. Mech. Phys. Solids* 49 (2001) 1747–1769.
- [4] I. Maskery, A.O. Aremu, M. Simonelli, C. Tuck, R.D. Wildman, I.A. Ashcroft, R.J.M. Hague, Mechanical properties of Ti-6Al-4V selectively laser melted parts with body-centred-cubic lattices of varying cell size, *Exp. Mech.* 55 (2015) 1261–1272.
- [5] M.P. Bendsoe, O. Sigmund, Material interpolation schemes in topology optimization, *Arch. Appl. Mech.* 69 (1999) 635–654.
- [6] P. Zhang, J. Toman, Y. Yu, E. Biyikli, M. Kirca, M. Chmielus, A.C. To, Efficient design-optimization of variable-density hexagonal cellular structure by additive manufacturing: theory and validation, *J. Manuf. Sci. Eng.* 137 (2015) (021004-1).
- [7] J. Robbins, S.J. Owen, B.W. Clark, T.E. Voth, An efficient and scalable approach for generating topologically optimized cellular structures for additive manufacturing, *Addit. Manuf.* 12 (2016) 296–304.
- [8] O. Sigmund, A new class of extremal composites, *J. Mech. Phys. Solids* 48 (2008) 397–428.
- [9] B. Zhu, M. Skouras, D. Chen, W. Matusik, Two-scale topology optimization with microstructures, *ACM Trans. Graph.* 36 (5) (2017) 164.
- [10] X.Y. Zheng, W. Smith, J. Jackson, B. Moran, H.C. Cui, D. Chen, J.C. Ye, N. Fang, N. Rodriguez, T. Weisgraber, C.M. Spadaccini, Multiscale metallic metamaterials, *Nat. Mater.* 15 (2016) 1100–1106.
- [11] H. Rodrigues, J.M. Guedes, M.P. Bendsoe, Hierarchical optimization of material and structure, *Struct. Multidiscip. Optim.* 24 (2002) 1–10.
- [12] L. Xia, P. Breitkopf, Concurrent topology optimization design of material and structure within FE2 nonlinear multiscale analysis framework, *Comput. Methods Appl. Mech. Eng.* 278 (2014) 524–542.
- [13] G.N. Wang, M.J. Pindera, Elasticity-based microstructural optimization: an integrated multiscale framework, *Mater. Des.* 132 (2017) 337–348.
- [14] J.D. Deng, J. Yan, G.D. Cheng, Multi-objective concurrent topology optimization of thermoelastic structures composed of homogeneous porous material, *Struct. Multidiscip. Optim.* 47 (2013) 583–597.
- [15] Y.Q. Wang, M.Y. Wang, F.F. Chen, Structure-material integrated design by level sets, *Struct. Multidiscip. Optim.* 54 (2016) 1145–1156.
- [16] J. Alexander, B.S. Lazarov, Topology optimization of manufacturable microstructural details without length scale separation using a spectral coarse basis preconditioner, *Comput. Methods Appl. Mech. Eng.* 290 (2015) 156–182.
- [17] H. Li, Z. Luo, N. Zhang, L. Gao, T. Brown, Integrated design of cellular composites using a level-set topology optimization method, *Comput. Methods Appl. Mech. Eng.* 309 (2016) 453–475.
- [18] H. Li, Z. Luo, L. Gao, P. Walker, Topology optimization for functionally graded cellular composites with metamaterials by level sets, *Comput. Methods Appl. Mech. Eng.* 328 (2017) 340–364.
- [19] Y.Q. Wang, F.F. Chen, M.Y. Wang, Concurrent design with connectable graded microstructures, *Comput. Methods Appl. Mech. Eng.* 317 (2017) 84–101.
- [20] S. Daynes, S. Feih, W.F. Lu, J. Wei, Optimisation of functionally graded lattice structures using isostatic lines, *Mater. Des.* 127 (2017) 215–223.
- [21] M.G. Rashed, M. Ashraf, R.A.W. Mines, P.J. Hazell, Metallic microlattice materials: a current state of the art on manufacturing, mechanical properties and applications, *Mater. Des.* 95 (2016) 518–533.
- [22] J.K. Liu, Y.S. Ma, A survey of manufacturing oriented topology optimization methods, *Adv. Eng. Softw.* 100 (2016) 161–175.
- [23] M. Kaur, T.G. Yun, S.M. Han, E.L. Thomas, W.S. Kim, 3D printed stretching-dominated micro-trusses, *Mater. Des.* 134 (2017) 272–280.
- [24] A. Takezawa, M. Kobashi, Y. Koizumi, M. Kitamura, Porous metal produced by selective laser melting with effective isotropic thermal conductivity close to the Hashin-Shtrikman bound, *Int. J. Heat Mass Transf.* 105 (2017) 564–572.
- [25] A. Cuadrado, A. Yáñez, O. Martel, S. Deviaene, D. Monopoli, Influence of load orientation and of types of loads on the mechanical properties of porous Ti6Al4V biomaterials, *Mater. Des.* 135 (2017) 309–318.
- [26] J. Schewardzgaier, F. Wein, G. Leugering, R.F. Singer, C. Körner, M. Stingl, F. Schury, Design of auxetic structures via mathematical optimization, *Adv. Mater.* 23 (2011) 2650–2654.
- [27] I. Ullah, J. Elambasseri, M. Brandt, S. Feih, Performance of bio-inspired Kagome truss core structures under compression and shear loading, *Compos. Struct.* 118 (2014) 294–302.
- [28] J. Bauer, S. Hengsbach, I. Tesari, R. Schwaiger, O. Kraft, High-strength cellular ceramic composites with 3D microarchitecture, *Proc. Natl. Acad. Sci. U. S. A.* 111 (7) (2014) 2453–2458.
- [29] Q.M. Wang, J.A. Jackson, Q. Ge, J.B. Hopkins, C.M. Spadaccini, N.X. Fang, Lightweight mechanical metamaterials with tunable negative thermal expansion, *Phys. Rev. Lett.* 117 (2016), 175901.
- [30] I. Maskery, N.T. Aboulkhair, A.O. Aremu, C.J. Tuck, I.A. Ashcroft, R.D. Wildman, R.J.M. Hague, A mechanical property evaluation of graded density Al-Si10-Mg lattice structures manufactured by selective laser melting, *Mater. Sci. Eng. A* 670 (2016) 264–274.
- [31] A.O. Aremu, J.P.J. Brennan-Craddock, A. Panesar, I.A. Ashcroft, R.J.M. Hague, R.D. Wildman, C. Tuck, A voxel-based method of constructing and skinning conformal and functionally graded lattice structures suitable for additive manufacturing, *Addit. Manuf.* 13 (2017) 1–13.
- [32] G. Allaire, F. Jouve, A.M. Toader, Structural optimization using sensitivity analysis and a level-set method, *J. Comput. Phys.* 194 (2004) 363–393.
- [33] M.Y. Wang, X.-M. Wang, D.-M. Guo, A level set method for structural topology optimization, *Comput. Methods Appl. Mech. Eng.* 192 (2003) 227–246.
- [34] A. Clausen, N. Aage, O. Sigmund, Exploiting additive manufacturing infill in topology optimization for improved buckling load, *Engineering* 2 (2016) 250–257.
- [35] A. Clausen, N. Aage, O. Sigmund, Topology optimization of coated structures and material interface problems, *Comput. Methods Appl. Mech. Eng.* 290 (2015) 524–541.
- [36] K. Svanberg, The method of moving asymptotes a new method for structural optimization, *Int. J. Numer. Methods Eng.* 24 (1987) 359–373.
- [37] J.P. Groen, O. Sigmund, Homogenization-based topology optimization for high-resolution manufacturable micro-structures, *Int. J. Numer. Methods Eng.* (2017) 1–16.
- [38] M.D. Zhou, B.S. Lazarov, F.W. Wang, O. Sigmund, Minimum length scale in topology optimization by geometric constraints, *Comput. Methods Appl. Mech. Eng.* 293 (2015) 266–282.
- [39] Q. Xia, T.L. Shi, Constraints of distance from boundary to skeleton: for the control of length scale in level set based structural topology optimization, *Comput. Methods Appl. Mech. Eng.* 295 (2015) 525–542.
- [40] Y.Q. Wang, L. Zhang, M.Y. Wang, Length scale control for structural optimization by level sets, *Comput. Methods Appl. Mech. Eng.* 305 (2016) 891–909.
- [41] Y.J. Luo, M.Y. Wang, Z. Kang, An enhanced aggregation method for topology optimization with local stress constraints, *Comput. Methods Appl. Mech. Eng.* 254 (2013) 31–41.
- [42] M. Bruggi, P. Venini, A mixed FEM approach to stress-constrained topology optimization, *Int. J. Numer. Methods Eng.* 73 (12) (2008) 1693–1714.
- [43] X.J. Gao, H.T. Ma, Topology optimization of continuum structures under buckling constraints, *Comput. Struct.* 157 (2015) 142–152.
- [44] A.G.M. Michell, The limit of economy of material in frame structures, *Philos. Mag.* 8 (6) (1904) 589–597.
- [45] O. Sigmund, N. Aage, E. Andreassen, On the (non-)optimality of Michell structures, *Struct. Multidiscip. Optim.* 54 (2016) 361–373.
- [46] P. Liu, Y.J. Luo, Z. Kang, Multi-material topology optimization considering interface behavior via XFEM and level set method, *Comput. Methods Appl. Mech. Eng.* 308 (2016) 113–133.